

Intra-urban nocturnal cooling rates: development and evaluation of the NOCRA model

Shiho Onomura,* Björn Holmer, Fredrik Lindberg and Sofia Thorsson

Department of Earth Sciences, University of Gothenburg, Sweden

ABSTRACT: A nocturnal cooling rate model (NOCRAM) to simulate nocturnal air temperature at urban sites is presented. The model is designed for urban planners, practitioners and researchers who demand meteorological information for urban planning and research applications. The model is based on the concept of nocturnal cooling, progressing in two distinct phases, i.e. site-dependent cooling around sunset and site-independent cooling from about 1 or 2 h after sunset until sunrise. Cooling rates are usually determined predominantly by prevailing weather conditions (i.e. clearness of the sky and wind speed), followed by maximum daily air temperature and by sky view factors. Second phase cooling is chiefly determined by sky clearness and wind speed. The findings and statistical results from the analysis of observational data during warm months (May–September) from Gothenburg, Sweden, as well as from past studies, were used. The model requires standard meteorological variables (i.e. wind speed, incoming short-wave radiation, air temperature, relative air humidity, air pressure) at a reference station as well as geometrical information (i.e. the sky view factor of the site and the geographical co-ordinates of the reference meteorological station). The model simulates the characteristic development of cooling rates in the two phases at open sites and built-up sites with different sky view factors under a wide range of weather conditions in warm months. Using the modelled cooling rates, nocturnal air temperature is estimated easily with the accuracy of root mean square error (RMSE) $\leq 1.54^\circ\text{C}$ and $R^2 \geq 0.78$.

KEY WORDS nocturnal cooling rate; two-phase cooling; intra-urban heat island; empirical modelling; urban planning applications

Received 11 September 2015; Revised 12 December 2015; Accepted 16 December 2015

1. Introduction

Night time air temperature is relevant to mortality risks particularly during persisting hot days, e.g. heat waves, as people recuperate during night from daytime heat stress (Rocklöv *et al.*, 2011; Laaidi *et al.*, 2012; Thorsson *et al.*, 2014). Urban development prone to lower night time air temperature can improve human thermal comfort within urban areas, consequently maintaining human health and well-being. However, urban built-up areas are apt to store heat. This leads to the so-called urban heat island (UHI) and the intra-urban heat island (IUHI) effects.

The UHI and IUHI are mainly nocturnal phenomena that develop through differences in cooling between urban and rural sites or between intra-urban sites of various types (Oke and Maxwell, 1975; Eliasson, 1994; Kidder and Essewanger, 1995; Runnalls and Oke, 2000). These differences are a result of variations in site characteristics such as building density, surface material, amount of vegetation and presence of anthropogenic heat (Oke, 1987). Nocturnal cooling progresses in two distinct phases (Oke and Maxwell, 1975; Upmanis *et al.*, 1998; Chow and Roth, 2006; Holmer *et al.*, 2007; Holmer *et al.*, 2013). In the late afternoon and evening (hereafter called Phase 1), the cooling rate at an urban/high-density site becomes less intensive than at a rural/open site, whereas in the night (i.e. approximately from

1 or 2 h after sunset, hereafter called Phase 2), cooling rates at the two sites converge on the same rate and decrease gradually until sunrise. The increasing spatial variation of air temperature in Phase 1 is a consequence of small-scale turbulence enhancing flux divergence locally, whereas the variation is maintained in Phase 2 due to turbulence breakdown (Acevedo and Fitzjarrald, 2001, 2003). Holmer *et al.* (2007) proposed the hypothesis that the Phase 1 cooling is dominated by radiative divergence and sensible heat flux, which are influenced by individual surface characteristics, whereas the site-independent cooling in Phase 2 is driven by radiative divergence in a capping inversion, which develops above the canopy layer.

The intensity of the UHI/IUHI or nocturnal cooling depends on external forcing, such as climate, weather and season, and also on the characteristics of the site. These relationships have been examined by many studies (e.g. reviewed by Arnfield, 2003; Unger, 2004). Among the external forcing, wind speed and cloud cover have been found to be the most significant meteorological variables governing the UHI/IUHI phenomenon. UHI/IUHI intensity decreases with increasing wind speed (e.g. Sundborg, 1951; Eliasson, 1996b; Morris *et al.*, 2001) as it enhances turbulent heat exchange and horizontal advection (Oke, 1987). Greater cloud cover reduces UHI/IUHI intensity (Kidder and Essewanger, 1995; Eliasson, 1996b; Magee *et al.*, 1999; Morris *et al.*, 2001) as clouds control the amount of incoming short-wave radiation heating the surface during daytime (Kawamura, 1964) and also reduce net long-wave radiation loss from the surface by absorbing out-going long-wave radiation and emitting it very efficiently back to the surface (Oke, 1987). Oke (1998) introduced an integrated weather factor that combined wind speed,

*Correspondence: S. Onomura, Gothenburg Urban Climate Group, Department of Earth Sciences, University of Gothenburg, Box 460, Gothenburg SE-405 30, Sweden. E-mail: shiho.onomura@gu.se

cloud cover and type, and it had a linear relationship with maximum UHI intensity (Runnalls and Oke, 2000). However, the practical use of the weather factor is limited as detailed cloud information is seldom available. Air temperature has also been used to explain the UHI intensity (Sundborg, 1951; Kawamura, 1964). Air temperature is correlated to seasonal variations in the intensity (Kawamura, 1964). Furthermore, the diurnal range of air temperature can be regarded indirectly as a measure of long-wave radiative loss from the ground (Kuttler *et al.*, 1996). Other external forcing such as air humidity (Kawamura, 1964) and air pressure (Moreno-Garcia, 1994) have also been reported to influence UHI/IUHI intensities.

Among the site characteristics, building density influences cooling rates by modifying out-going long-wave radiation and turbulent heat exchange (Oke, 1981; Johnson, 1985). With higher building density, expressed as the sky view factor (SVF) or the height-to-width ratio (H/W), UHI/IUHI intensities increase while cooling rates are less intensive (e.g. Oke, 1981; Johnson, 1985; Unger, 2004). Surface materials also modify cooling rates as differences in surface radiative properties and thermal admittance change sensible heat flux and the outgoing long-wave radiation released into the atmosphere (Oke, 1988). Although the influence of different surface materials is as significant as building density (Oke *et al.*, 1991; Eliasson, 1996a), some studies report that cooling rates or UHI/IUHI intensities indicating the amount of nocturnal transported heat have a high correlation with SVF, e.g. $R^2 > 0.8$ (Oke, 1981; Konarska *et al.*, 2015a). Oke (1981) suggests that SVF explains most of IUHI intensities given similar surface materials within a single urban area but Konarska *et al.* (2015a) found that SVF is the most important factor controlling cooling rates even in comparison between non-vegetated sites and vegetated sites. As described above, the physical concepts of UHI/IUHI intensities and cooling rates and their relationships with meteorological variables and site characteristics have been established. They can be used for the modelling of nocturnal air temperature.

Nowadays, there are several models that can simulate air temperature in the urban canopy layer (e.g. Swaid and Hoffman, 1990; Erell and Williamson, 2006; Harman and Belcher, 2006; Bohnenstengel *et al.*, 2011; Bueno *et al.*, 2013), but most of them aim for scientific uses and are not suitable for practical uses due to their model complexity and input requirements. With relatively fewer requirements, the analytical model of Erell and Williamson (2006) and the urban canopy model of Bueno *et al.* (2013) can be used as practical tools. However, the surface schemes in the models still require detailed information about buildings and surface characteristics. For urban planners and practitioners, it is still not straightforward to quantify the importance of specific factors such as site characteristics and weather situations and how they influence cooling at an urban site.

In this study, an intra-urban nocturnal cooling rate model is developed to calculate night-time air temperature in the urban area. This model is suitable for urban planners and practitioners who demand information on cooling rates as well as intra-urban air temperature in urban planning applications. The model is based on the established two-phase cooling concept (Acevedo and Fitzjarrald, 2001, 2003; Holmer *et al.*, 2007). Observational data from non-vegetated sites in Gothenburg, Sweden, are used to investigate the onset of the two phases as well as the relationships between cooling rates and meteorological variables and building density (SVF). The influences of surface material on cooling rates are not taken into account as the sites are covered mostly by standard urban fabrics (asphalt and brick). The findings and statistical results as well as knowledge from previous studies are

used for the model's development. The model requires only standard meteorological variables from a nearby reference meteorological station, geometrical information about the calculated SVF of the site and geographical co-ordinates of the reference station. The model performance is evaluated with additional observation data from Gothenburg and London, UK.

2. Study site and observational data

The city of Gothenburg ($57^\circ 42' N$, $11^\circ 58' E$) is located on the Swedish west coast. It is the second largest city in Sweden with a population of 541 000 (SCB, 2014). The city was founded in 1623 and its central part is dense, mostly with 3–6 story buildings. The city has a marine temperate climate (Cfb) according to the Köppen climate classification, characterized by relatively cool summers and mild winters.

For the model development, a meteorological dataset (Thorsson and Eliasson, 2003) containing air temperature measured between May and September in 1999 at an open site with asphalt and gravel (named GOT098, where the three letters are the code of the city and the three digits show the SVF of 0.98) and in a narrow street paved with asphalt, surrounded by mid-rise brick buildings (GOT039) in the city centre (Figure 1(a)) was used. Air temperature was measured using TinyTag loggers (Gemini Data Loggers, Chichester, UK) with an accuracy of $\pm 0.2^\circ C$ between $0^\circ C$ and $70^\circ C$. They were sheltered with radiation shields and mounted at 2 m above the ground. Air temperature was also measured at 10 m at the GOT098 site. At this site, wind speed was measured as 4.5 m and 10 m using a Gill ultrasonic anemometer (accuracy of $\pm 3\%$) and a Vaisala WAA15 anemometer (accuracy of $\pm 0.1 \text{ m s}^{-1}$), respectively. Air pressure was taken from a meteorological station at an airport located 12 km northwest of the GOT098 site operated by the Swedish military weather service (Figure 1(b)). Other meteorological variables such as global radiation, precipitation and relative humidity were taken from a meteorological station 1 km north of the GOT098 site operated by the Swedish Meteorological and Hydrological Institute (SMHI). The clearness index of the sky was calculated to account for cloud conditions (see Section 3.3.1). The index was compared with the cloudiness (oktas) observed visually at the airport.

For the model evaluation, two independent datasets were prepared, one from Gothenburg and one from London, UK, which has the same climate class (Cfb). For Gothenburg, an air temperature dataset (Konarska *et al.*, 2015a) covering May to September in both 2012 and 2013 at an open site paved with asphalt (GOT092) and at a built-up site (GOT040) similar to the GOT039 site was used (Figure 1(a)). The same type of sensor was used, but the measurement height was 2.2 m, i.e. slightly higher than the former dataset. Meteorological input variables (air pressure, global radiation, precipitation, relative humidity and wind speed) were taken from a roof-top meteorological station located 30 m above the ground and 2 km southwest of the GOT098 site (GVC, 2014) (Figure 1(b)). For London, air temperature covering June to September in 2014 at a built-up site with little vegetation and paved with dark-coloured tiles (LDN046, $51^\circ 31' N$, $0^\circ 5' W$) (London Urban Micrometeorological data Archive (LUMA, 2014)) located in the Barbican Estate was used. The estate has complex urban settings, unlike Gothenburg's built-up sites, and a large variation in building height. The air temperature was measured using a Davis sensor, located 4 m above the ground. Similarly, the meteorological input data were taken from a nearby meteorological station (LUMA, 2014) located 128 m above the ground, 0.1 km east of the LDN046 site. As a standard for input wind speeds, the

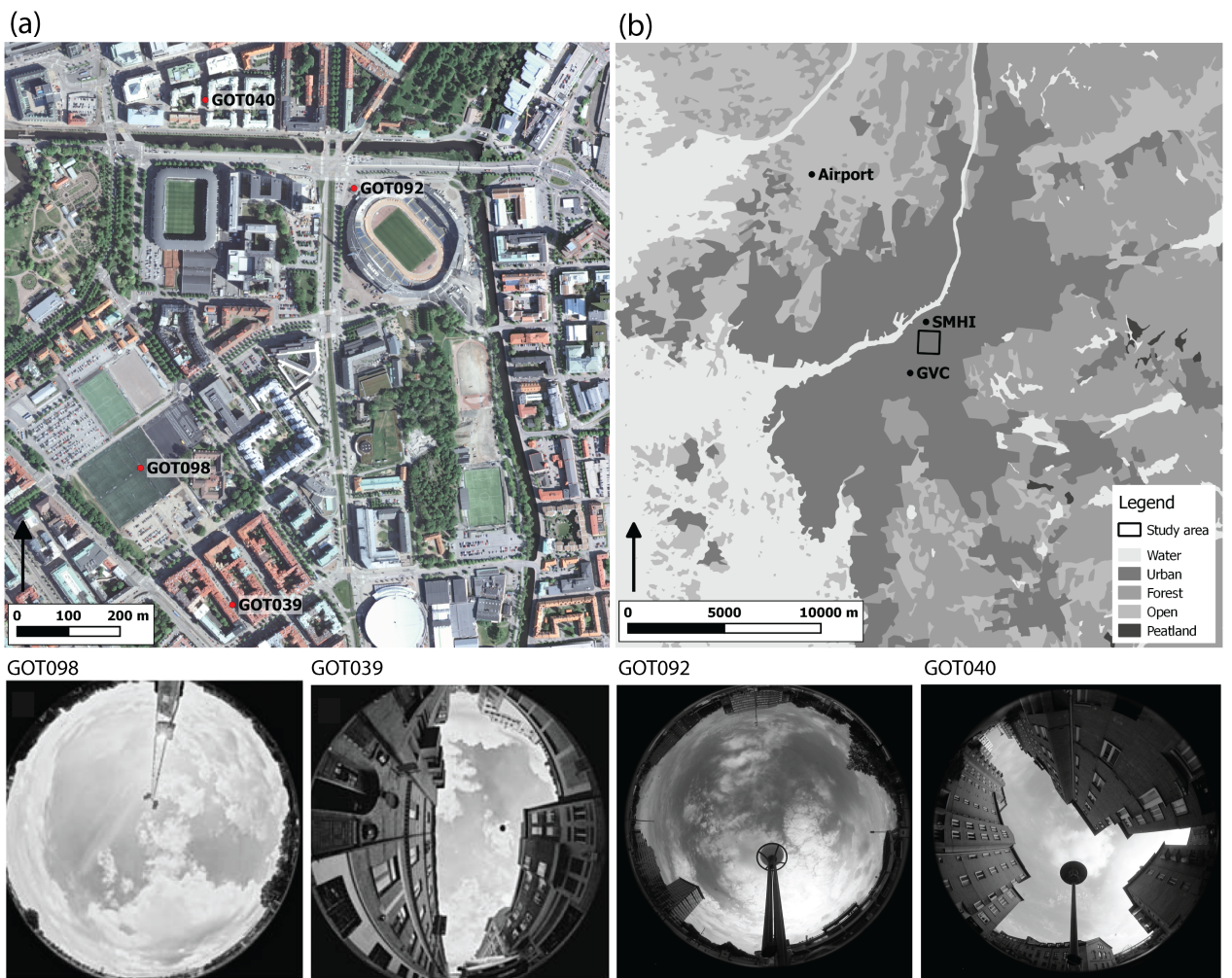


Figure 1. (a) Location of study sites in the centre of Gothenburg and (b) meteorological stations around the study area. Fish-eye photographs from the sites are shown at the bottom.

height was set as 10 m. The meteorological stations in Gothenburg and London are located higher than 10 m. Therefore, the wind speeds were adjusted to the standard height using the wind power law with the exponential co-efficient of 0.286 (Davenport, 1960) for the Gothenburg sites and 0.302 for the London site, which is estimated using the wind speeds of the meteorological station and the LDN046 site.

Sunset (sunrise) was defined by when the global radiation is less (more) than 10 W m^{-2} . All the data had 30 m time resolution. To avoid the effect of cooling driven by evaporation and/or synoptic weather changes, only days with accumulated precipitation $<0.5 \text{ mm}$ and a daily pressure change $<10 \text{ hPa}$ from noon to sunrise (66 days for the former dataset and 194 days for the latter dataset of Gothenburg and 79 days for the London dataset) were used. The hourly cooling rate (K h^{-1}) was calculated using the air temperature.

The total SVF, characterizing both buildings and vegetation (trees and bushes) within the study area, was calculated using digital surface models (DSMs) of buildings and vegetation using the solar and long-wave environmental irradiance geometry (SOLWEIG) 2013a model (Lindberg *et al.*, 2008; Lindberg and Grimmond, 2011a) as described by Lindberg and Grimmond (2010). The DSMs have a spatial resolution of 1 m. The SVF representing each site was taken to be the average SVF of ground surface (thus excluding roof surfaces) within a 25 m radius,

calculated using the ArcMap 10.1 software. The circular size was determined based on the study of Konarska *et al.* (2015a), which showed that average SVF within a 25 m circular area has a strong relation to the most intensive cooling rate in Phase 1.

The influence of evapotranspiration from vegetation or natural surfaces on cooling rates was ignored. Compared with the radiative effect of trees and bushes obscuring the sky, the evapotranspiration effect was found to be less significant (Spronken-Smith and Oke, 1998; Konarska *et al.*, 2015a). The impact of anthropogenic heat was also ignored as coolers/heaters are not commonly used in Sweden between May and September.

3. Model development and description

3.1. Outline of the model structure

The nocturnal cooling rate model (NOCRM) estimates a profile of nocturnal cooling rate based on the two-phase cooling concept. As an example, a conceptual profile typical of open sites under ideal (clear and calm) conditions is depicted in Figure 2. The temporal development of cooling rates is partitioned into Phases 1 and 2, and Phase 1 is further divided into two parts (1A and 1B). Phases 1A and 1B are modelled with cosine functions using the initial cooling rate (CR_1) of Phase 1A, the most intensive cooling rate (CR_{peak}) and initial cooling rate (CR_2) of Phase 2 and

the timing of Phases 1A, 1B and 2 (t_1 , t_{peak} and t_2). The angles applied to Phases 1A and 1B range from 0 to π and π to 2π , respectively. CR_1 is determined by the end of daytime cooling (see Section 3.2), which is not simulated in this model. Thus, CR_1 is provided by observed air temperatures, and t_{peak} is calculated simply as the mid time between t_1 and t_2 , though either positive or negative deviation from the mid time is seen in previous studies (e.g. Holmer *et al.*, 2013). It was expected that t_{peak} can also be detected based on a thermodynamic process, e.g. by using an atmospheric stability index (see Section 3.5), but the method was not used in the present model as the index requires data from specialized measurements. The t_1 , t_2 , CR_{peak} and CR_2 are determined using meteorological variables and SVF (Sections 3.2–3.4). Phase 2 is modelled with a linear function using CR_2 and t_2 under the assumption that cooling ends at sunrise ($= t_{\text{end}}$). Lastly, the profile is modified at every time step by estimating the impact of wind disturbance on cooling rates (sketched in Figure 2 and explained in Section 3.5).

3.2. Determination of the timing of Phases 1A and 2

Figure 3(a)–(d) shows a temporal series of air temperature and cooling rate at an open site (GOT098) and a built-up site (GOT039), wind speed (10 m), relative wind speed change and the bulk Richardson number on a clear day for 27 and 28 July 1999. Relative wind speed change is defined as the ratio of wind speed change *per hour* to the hourly average wind speed, which is used to show turbulence structure. The bulk Richardson number (Ri_b), an atmospheric stability index, was calculated based on the equation in Golder (1972) using air temperature measured at two levels (2 and 10 m) and wind speed at 4.5 m at the GOT098 site.

Cooling started in the middle of the afternoon after the air temperature reached its maximum (line A in Figure 3(a)). Phase 1 started when the cooling rates diverged between the sites (line B in Figure 3(b)). Phase 2 started about 1.5 h after sunset, when the cooling rates at the two sites converged again on the same rate (line D in Figure 3(b)). Abrupt wind speed decay occurred (Figure 3(c)), and Ri_b turned from negative to positive (Figure 3(d)) in Phase 1, while in Phase 2 wind ceased and Ri_b stayed at positive values. The temporal variations are linked to the decay of turbulence, and it is suggested that the start of the early evening transition (corresponding to Phase 1) could be determined by the time when wind speed decreases from mid-afternoon values (Acevedo and Fitzjarrald, 2001). An attempt was made to detect the onset of Phases 1A and 2 using relative wind speed change.

The cooling before Phase 1 (between line A and B in Figure 3(b)), named daytime cooling, has more or less the same rates between the two sites. During the site-independent cooling, wind speed remained as high as in the middle of the day (Figure 3(c)), and Ri_b was negative (Figure 3(d)). This indicates the existence of large-scale daytime turbulence, which transports heat predominantly by vertical mixing and advection. The cooling is also attributable to long-wave radiative divergence influenced by site characteristics, but due to the large extent of daytime turbulence across the two sites, the cooling rates are almost the same.

When Phase 1 started (line B in Figure 3(b)), relative wind speed change was <-0.2 (Figure 3(c)). The value was employed to determine t_1 in the model. Specifically t_1 is set to the time between 3.5 h before sunset to sunset when relative wind speed change falls below -0.2 and is also negative in the previous time step. The negative pulse marks the change of wind structure from large-scale daytime turbulence to smaller-scale turbulence

enhancing heat exchange locally, which results from decreasing sensible heat flux from the surface. Thus, both turbulent transfer and long-wave radiative divergence influenced by the site characteristics encouraged the cooling to be site-dependent as well as more intensive.

Approximately 1 h before the start of Phase 2, wind speed fell to 0.05 m s^{-1} , and relative wind speed change was the most negative (-1.7) (Figure 3(c)), indicating that turbulence was broken down. In fact, on most days, relative wind speed change fell only below around -0.5 . Therefore, in the model, the onset of Phase 2 (t_2) is determined as 1 h after the time between 1 h before sunset and 4 h after sunset when relative wind speed change falls below -0.5 . If t_2 is earlier than t_1 , t_2 is set to be the next time step of t_1 . In Phase 2, a strong inversion layer is established with positive Ri_b (Figure 3(d)), and the cooling rate decreases gradually at the same constant rate at both the sites until sunrise (Figure 3(b)).

Default values are prepared for the case when t_1 and t_2 cannot be determined because relative wind speed change does not meet the conditions. According to average profiles of cooling rates (not shown) at the open and built-up sites, t_1 and t_2 were detected -2 h and 2 h from sunset, respectively, under clear conditions (defined as the clearness index of the sky (CI) ≥ 0.9 ; the CI calculation is explained in Section 3.3.1). Under semi-cloudy conditions ($\text{CI} < 0.9$ and ≥ 0.75), t_1 and t_2 were -1 h and 1 h , respectively, but under cloudy conditions ($\text{CI} < 0.75$), they were hardly detected. The results imply that the length of Phase 1 becomes shortened as CI becomes lower. Therefore, the default values of t_1 and t_2 are set to be -2 h and 2 h from sunset, respectively, when $\text{CI} = 1$, and the time from sunset decreases linearly as CI become lower.

3.3. Determination of most intensive cooling rate

CR_{peak} is estimated by first considering the impact of weather conditions and seasonality, followed by the impact of building density.

3.3.1. Influence of weather conditions and seasonality

Data from the open site (GOT098) were used to investigate the influence of weather conditions and seasonality on CR_{peak} for open sites ($\text{CR}_{\text{peak, open}}$).

As mentioned above, Oke (1998) proposed a weather factor that combines wind speed and cloud cover/type, which is approximately linearly related to maximum nocturnal UHI intensity (Runnalls and Oke, 2000). The factor ranges from 0 (overcast and windy condition) to 1 (clear and calm). It expresses the degree to which the weather conditions reduce the potential UHI intensity under the ideal condition (the factor is 1). There are two practical issues to use the weather factor proposed by Oke (1998) directly to estimate the effect of the weather conditions on cooling rates. First, cloud information (cover and type) is rarely available. Secondly, the limit of the lowest wind speed is set to 1 m s^{-1} . According to the present study's data analysis, the magnitude of $\text{CR}_{\text{peak, open}}$ increases with lower wind speed, at speeds $< 1 \text{ m s}^{-1}$. In order to address these shortcomings, a new weather factor, named cooling rate impact factor (CRIF), was introduced. The new factor is similar to the one of Oke (1998) but more suitable for the CR_{peak} estimation. It consists of wind speed and CI of the sky instead of cloud cover and type. CI was calculated as the ratio of measured solar irradiance to the clear-sky irradiance based on the Crawford and Duchon (1999) method, modified by Lindberg and Grimmond (2011b) to correct for the underestimation of CI when the Sun's altitude is low. As it denotes the amount of incoming short-wave radiation across the atmosphere, it can be

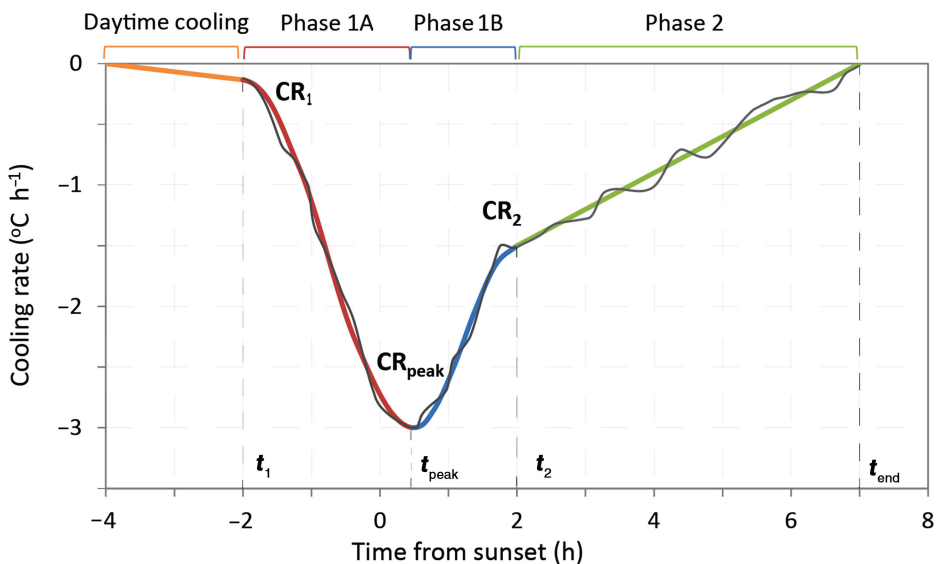


Figure 2. A conceptual profile of the cooling rate for open sites under ideal (clear and calm) conditions. The start and end of Phases 1A, 1B and 2 are indicated by t_1 , t_{peak} , t_2 and t_{end} . Initial cooling rate in Phase 1A (CR_1), most intensive cooling rate (CR_{peak}) and initial cooling rate in Phase 2 (CR_2) are shown. A thin line around the profile illustrates how weather changes such as wind and cloud cover/type affect cooling rates during night.

used to show the impact of not only cloud amount but also different types of clouds blocking incoming and outgoing radiation on cooling rates. The calculation requires standard meteorological variables, i.e. global radiation, air temperature, relative humidity and air pressure. A disadvantage of using the index is that it is available only for the daytime. Therefore, for nocturnal cloud conditions, the calculated CIs between noon and sunset and for 3 h after sunrise on the next day, and thus across the night, were used. The CIs were compared with the observed cloud cover (n) (oktas) by using box plots in Figure 4. The median of the CI is approximately proportional to $1 - 0.6(n/8)^2$, which is similar to an index of cloudiness used in the weather factor of Oke (1998). This means that CI can be a replacement for cloud cover and type. Wind speed in CRIF appears in the form of a negative square root instead of the inverse square root used in Runnalls and Oke (2000) because the magnitude of CR_{peak} was found to decrease with the negative square root of average wind speed for ± 3 h around the time when the cooling rate is the most intensive (U_1). Therefore, CRIF is expressed as:

$$\text{CRIF} = \left(1 - \sqrt{\frac{U_1}{U_{\text{crit}}}}\right) \frac{(\text{CI} - \text{CI}_{\min})}{(\text{CI}_{\max} - \text{CI}_{\min})} \quad (1)$$

where CI is the average between noon and sunset and for 3 h after the sunrise on the next day (hereafter, CI means the average value). Figure 5 visualizes this index that takes the value of 1 under clear sky ($\text{CI} = 1$, named CI_{\max}) and calm ($U_1 = 0$) conditions and decreases as CI decreases and U_1 increases. CRIF is 0 when CI is below a critical value (CI_{\min} set to 0.4) and/or U_1 exceeds a threshold value (U_{crit} set to 4 m s^{-1}). The value of CI_{\min} is determined by the fact that $\text{CI} = 0.4$ corresponds approximately to the median for eight oktas cloud cover (completely overcast) in Figure 4, and the impact of changes in a further lower CI on cooling rates can be neglected. Figure 6 shows that $\text{CR}_{\text{peak}, \text{open}}$ is approximately related linearly to CRIF, with $R^2 = 0.52$. The considerable amount of scatter can be attributed to the influence of other external forcings such as seasonal variations in solar insolation and the advection of cooler/warmer air and water vapour from the surrounding.

Maximum daily air temperature (T_{\max}) can be a measure of the surface energy balance associated with cooling rate, i.e. high T_{\max} is attributed to large sensible heat and outgoing long-wave radiation following high solar insolation and large surface heat storage. As a result, the effect of seasonal variations in the surface energy balance on cooling rates can be taken into account by using T_{\max} . Figure 7 shows that the magnitude of $\text{CR}_{\text{peak}, \text{open}}$ increases with higher T_{\max} for the two classes of $\text{CRIF} \geq 0.35$ and < 0.35 (determined as about the half of maximum CRIF in the observation, see Figure 6). The fitted lines for the two classes show the same rate of $\text{CR}_{\text{peak}, \text{open}}$ changes with T_{\max} , but the trend for $\text{CRIF} < 0.35$ is less reliable due to less data when $T_{\max} > 20^\circ\text{C}$. In order to relate T_{\max} to CR_{peak} , two assumptions were introduced. First, the slope and intercept of the linear relationship assumed to be between $\text{CR}_{\text{peak}, \text{open}}$ and T_{\max} scales with CRIF. Secondly, at $\text{CRIF} = 0$ (overcast and windy condition), $\text{CR}_{\text{peak}, \text{open}}$ does not change with T_{\max} and is equal to the minimum value of $\text{CR}_{\text{peak}, \text{open}}$ set to -0.2 K h^{-1} . Based on the assumptions, CR_{peak} for open sites can be expressed as a function of T_{\max} and CRIF:

$$\text{CR}_{\text{peak}, \text{open}} = -0.2 - 0.14 \cdot \text{CRIF} \cdot (T_{\max} + 9.14) \quad (2)$$

where $\text{CR}_{\text{peak}, \text{open}}$ is set to -0.2 for all CRIF cases if $\text{CR}_{\text{peak}, \text{open}} > -0.2$. The relationship is depicted by gray lines in Figure 7 for CRIF from 0 to 1.

3.3.2. Influence of building density

Subsequently, the influence of SVF on CR_{peak} is estimated by introducing the sky view impact factor (SVIF), which is defined as the rate of reduction in CR_{peak} at a built-up site ($\text{CR}_{\text{peak}, \text{built-up}}$) compared with that at an open site ($\text{SVF} = 1$) ($\text{CR}_{\text{peak}, \text{open}}$). CR_{peak} can be assumed to decrease linearly with lower SVF as many past studies have reported that UHI/IUHI intensities decrease with higher SVF (see the reviews of Unger, 2004). SVIFs for the built-up site (GOT039) compared with the open site (GOT098) were calculated for $\text{CRIF} \geq 0.35$ and < 0.35 and plotted with the SVF in Figure 8. SVIF decreasing with lower CRIF indicates that the influence of SVF on CR_{peak} decreases

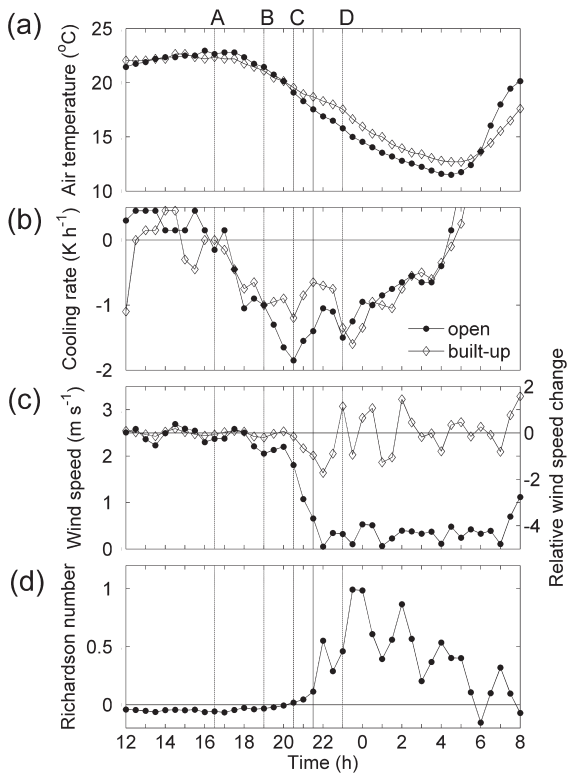


Figure 3. A temporal series of (a) air temperature, (b) cooling rate for an open (black dot) and a built-up (diamond marker) sites, (c) wind speed (black dot) and relative wind speed change (the ratio of wind speed *per hour* to hourly average wind speed) (diamond) and (d) the bulk Richardson number on 27 and 28 July 1999. Time resolution is 30 min. A vertical light-grey line corresponds to the sunset and four dashed lines indicate (A) the start of daytime cooling, (B) the start of Phase 1, (C) the time of most intensive cooling rate and (D) the start of Phase 2.

under cloudier and windier conditions. The trend was confirmed with the other built-up sites studied by Thorsson and Eliasson (2003) and Holmer *et al.* (2007). Therefore, assuming that the linear relationship between SVIF and SVF scales with CRIF, SVIF is expressed as:

$$\text{SVIF} = \frac{\text{CR}_{\text{peak, open}} - \text{CR}_{\text{peak, built-up}}}{\text{CR}_{\text{peak, open}}} = (1 - \text{SVF}) \cdot \text{CRIF} \quad (3)$$

which is shown graphically in Figure 8 for CRIF from 0 to 1.

Using SVIF, CR_{peak} for any site is expressed as:

$$\text{CR}_{\text{peak}} = \{-0.2 - 0.14 \cdot \text{CRIF} \cdot (T_{\max} + 9.14)\} (1 - \text{SVIF}) \quad (4)$$

3.4. Determination of initial cooling rate in Phase 2

When Phase 2 starts (t_2), the cooling rate (CR_2) is determined by the intensity of the thermal stratification of the stable atmosphere and by the strength of vertical mixing to transport warmer air into the roughness sublayer. The impact of hourly averaged wind speed (U_2) at t_2 on CR_2 is examined for the two classes of $\text{CI} > 0.9$ (clear conditions) and $\text{CI} < 0.6$ (cloudy conditions) (Figure 9). The fitting lines for the two classes show that the magnitude of CR_2 decreases with higher U_2 under clear conditions, while under cloudy conditions, the magnitude changes little with U_2 . The impact of vertical mixing on cooling rates is larger in a more stable atmosphere, developed favourably under clear conditions. The result suggests that CR_2 is determined predominately

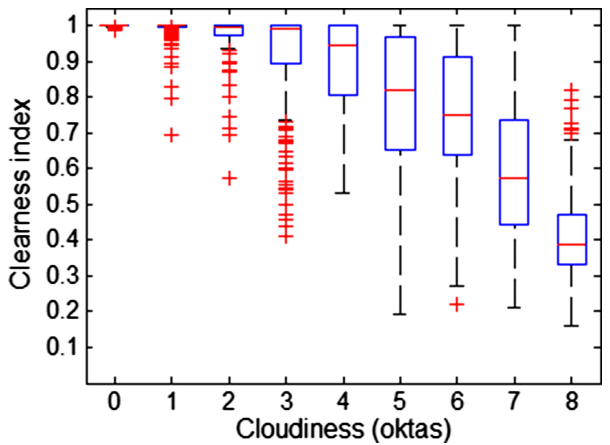


Figure 4. The relationship between observed cloudiness and clearness index of the sky calculated with observed global radiation, air temperature, relative humidity and air pressure. The bottom and top edges of the box show the 25th and 75th percentiles of the data, and the line in the box is the median.

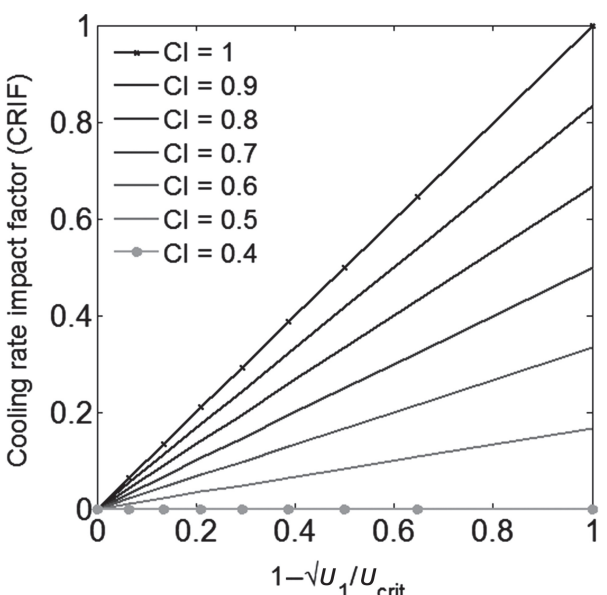


Figure 5. Cooling rate impact factor in relation to clearness index of the sky (CI) and average wind speed (U_1) for ± 3 h around the time of the most intensive cooling. Critical wind speed (U_{crit}) is set to 4 m s^{-1} .

by CI and U_2 . Assuming that the relationship between CR_2 and U_2 scales linearly with CI when $\text{CI} \geq 0.5$, but when $U_2 \geq 2 \text{ m s}^{-1}$ CR_2 follows the line of $\text{CI} = 0.5$ (i.e. $\text{CR}_2 = -0.3$) and that when $\text{CI} < 0.5$, the magnitude of CR_2 decreases linearly with CI regardless of U_2 , CR_2 is expressed as:

$$\text{CR}_2 = \begin{cases} -0.3 - 1.7 \frac{(2-U_2)}{2} \frac{\text{CI}-0.5}{1-0.5} & \text{if } \text{CI} \geq 0.5 \text{ and } U_2 \leq 2 \\ -0.3 & \text{if } \text{CI} \geq 0.5 \text{ and } U_2 > 2 \\ -0.3 - 0.5(\text{CI} - 0.5) & \text{if } \text{CI} < 0.5 \end{cases} \quad (5)$$

The relationship is shown in Figure 9 for CI from 0.4 to 1.

3.5. Modelling the impact of wind disturbance

Given no horizontal advection, cooling rates are influenced particularly by vertical mixing of the air and cloudiness. The impact

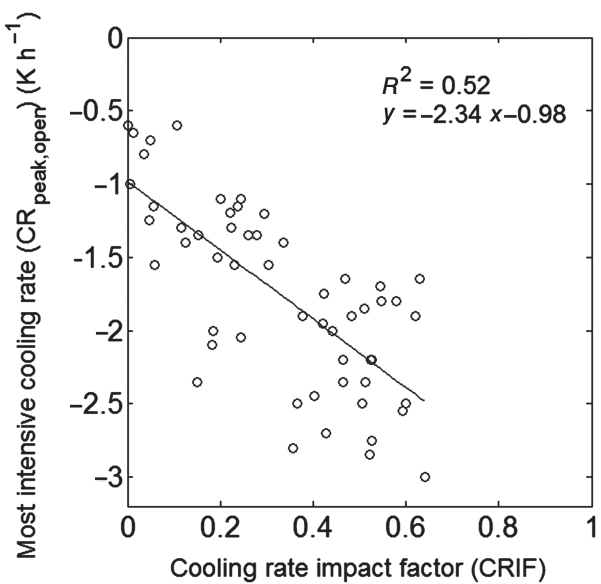


Figure 6. The most intensive cooling rate with cooling rate impact factor for an open site (GOT098) in Gothenburg during May–September 1999.

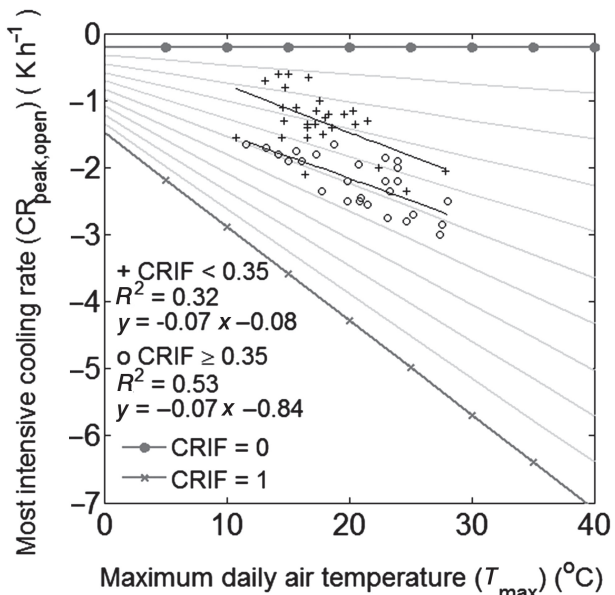


Figure 7. The most intensive cooling rate with maximum daily air temperature for two classes of cooling rate impact factor (CRIF) (circle: ≥ 0.35 and cross: < 0.35) for an open site (GOT098) in Gothenburg during May–September 1999. Grey lines show the relationship between CR_{peak} and T_{max} scales linearly with CRIF from 0 to 1.

of the mixing driven by wind disturbance is considered in the model but that of cloudiness changes is not as CI is not available during the night. An increase in the large-scale wind causes the stable surface layer to reconnect to the upper layer (Acevedo and Fitzjarrald, 2003). Acevedo and Fitzjarrald (2003) suggest that wind speed above a threshold of 1.5 m s^{-1} drives turbulent flux exchange between the canopy layer and the upper layer, while a lower wind speed promotes mixing the air down to the cold ground. On the basis of the concept, the present study hypothesized that wind speed higher than the average value of the phase drives turbulent exchanges between the roughness sublayer and the upper layer, whereas a lower wind speed exchanges the air

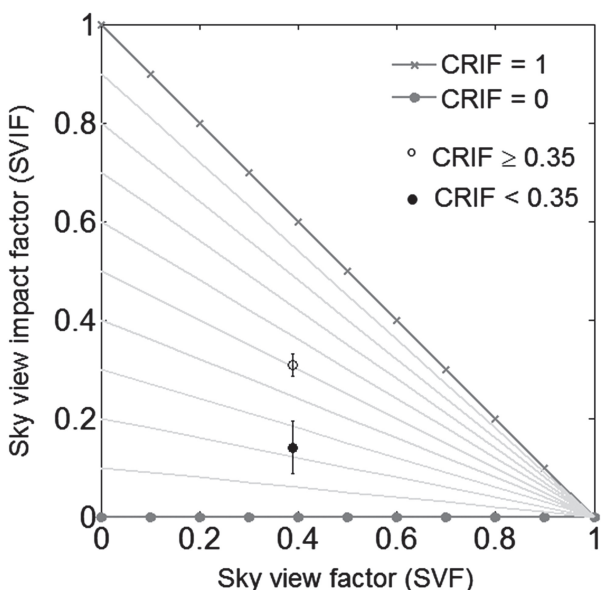


Figure 8. Determination of the sky view impact factor (SVIF) using the sky view factor (SVF) and cooling rate impact factor (CRIF). SVIF is defined as the rate of reduction in the most intensive cooling rate at a built-up site compared with an open site. Two circle points show average SVIFs for $CRIF < 0.35$ (filled) and ≥ 0.35 (open) calculated for a built-up site ($SVF = 0.39$) compared with an open site ($SVF = 0.98$) in Gothenburg during May–September 1999. A vertical line on each point shows the standard deviation.

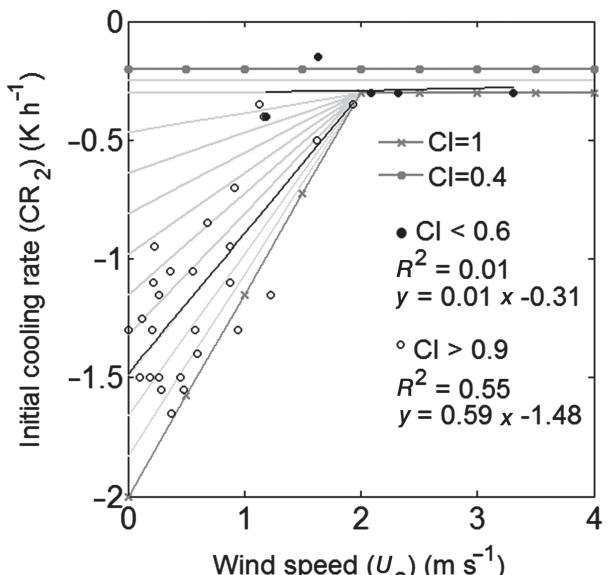


Figure 9. Determination of the initial cooling rate of Phase 2 using hourly averaged wind speed at the start of Phase 2 (U_2) and clearness index of the sky (CI) in Gothenburg during May–September 1999. The trend line and co-efficient of determination (R^2) for each CI class are shown.

between the roughness sublayer and near surface. The impact of heat exchange driven by wind speed changes is estimated specifically for every time step as a function of the square root of the difference between wind speed at the time step and the average wind speed of the phase ($\bar{U}_{\text{Phase 1A}}$, $\bar{U}_{\text{Phase 1B}}$ and $\bar{U}_{\text{Phase 2}}$). The square root form is based on the fact that the magnitude of cooling rate is related to the square root of wind speed (Section 3.3.1).

Furthermore, the influence of wind speed changes can vary with vertical thermal distribution of the air, i.e. the atmospheric stability. In Figure 3, the change in the sign of Ri_b was found to correspond roughly to the time when the most intensive cooling rate occurred, i.e. 1 h before sunset (line C in Figure 3(d)). In Phase 1A (lines B–C), Ri_b turned from negative (-0.032) to nearly zero (-0.0068), while it became positive (0.019) at the start of Phase 1B and continuously increased towards Phase 2. An additional analysis using all other days shows that the time of a change in the sign of Ri_b occurs most frequently (65%) within 1 h from the time when cooling is the most intensive (Figure S1). This implies that outgoing sensible heat encourages the cooling in the roughness sublayer in Phase 1A, whereas in Phase 1B, incoming sensible heat from above diminishes the cooling driven by radiative divergence. Therefore, wind speed above the average wind speed of the phase brings colder air from above the roughness sublayer and enhances cooling rates in Phase 1A, whereas it brings warmer air from above and diminishes cooling rates in Phases 1B and 2. The case of a lower wind speed than the average is the other way around. Lastly, the magnitude of the wind impact on cooling rates is adjusted with the strength of thermal stratification of the atmosphere. This is conducted by introducing the wind impact factor (WIF) which expresses the influence of the strength of the thermal stratification from 0 to 1 using CI. Based on the sensitivity test (not shown), WIF changes from 0.1 to 0.35 as CI varies from 0.4 to 1. Finally, the deviation of the cooling rate caused by wind disturbance at time t ($\Delta CR_w(t)$) is expressed as:

$$\Delta CR_w(t) = \begin{cases} -WIF\sqrt{|U(t) - \bar{U}_{Phase,x}|} & \text{if } x = 1A \\ +WIF\sqrt{|U(t) - \bar{U}_{Phase,x}|} & \text{if } x = 1B \text{ or } 2 \end{cases} \quad (6)$$

when $U(t) > \bar{U}_{Phase,x}$. The plus and minus signs before WIF are reversed when $U(t) < \bar{U}_{Phase,x}$.

3.6. Summary of modelling

With all the parameters determined above, nocturnal cooling rates (CR) are calculated. For Phase 1A, using CR_1 , CR_{peak} , $\Delta CR_w(t)$ and function f that converts time into radian (0 to π), CR is modelled as follows:

$$\begin{aligned} CR = & (CR_1 - CR_{peak}) (\cos(f(t - t_1)) - 1) / 2 \\ & + CR_1 + \Delta CR_w(t) \\ & \text{when } t_1 \leq t < t_{peak} \end{aligned} \quad (7)$$

For Phase 1B, using CR_2 , CR_{peak} , $\Delta CR_w(t)$ and the function f for π to 2π , CR is modelled as:

$$\begin{aligned} CR = & (CR_2 - CR_{peak}) (\cos(f(t - t_{peak})) + 1) / 2 \\ & + CR_{peak} + \Delta CR_w(t) \\ & \text{when } t_{peak} \leq t < t_2 \end{aligned} \quad (8)$$

Lastly, CR in Phase 2 is determined using CR_2 and $\Delta CR_w(t)$ as follows:

$$\begin{aligned} CR = & \frac{t_{end} - t}{t_{end} - t_2} CR_2 + \Delta CR_w(t) \\ & \text{when } t_2 \leq t \leq t_{end} \end{aligned} \quad (9)$$

4. Model evaluation

4.1. Evaluation for specific days

Time series of modelled and observed cooling rates for an open site (GOT098) on 2 days (28 July and 22 June) were investigated together with air temperature, wind speed, relative wind speed change and wind direction (Figure 10). The 2 days represent a case of well-modelled and poorly modelled cooling, respectively. In order to examine the timing of t_1 and t_2 , observed cooling rates for a built-up site (GOT039) are also shown.

On 28 July, when a typical cooling with the two distinct phases under clear and calm condition prevailed, the model simulated the temporal development of cooling rates well. The magnitude of CR_{peak} was modelled reasonably. The timing of t_1 and t_2 corresponded to the observation, though t_{peak} was 30 min later than the observation. It is probably attributed to the simplified calculation of t_{peak} . However, despite this, the characteristics of intensive cooling during Phase 1 were captured well. The model was particularly successful to simulate cooling rates in Phase 2 influenced by changes in wind speed, which are seen in good agreement with the observation.

On the other hand, the model sometimes did not capture the observational cooling. The example case is 22 June, which has a complex temporal development of observed cooling rates. Phase 1 is simulated well with reasonably estimated t_1 and CR_{peak} , whereas Phases 1B and 2 are either over-estimated or under-estimated. In the observation, relatively high wind speed for 2 h after sunset interrupts the stabilization of the atmosphere in Phases 1B and 2 and diminishes the magnitude of cooling rates. Wind speed ceases rather late, 4 h after sunset when wind direction changes from the west to the east (from sea breeze to land breeze). At the same time, the observed cooling becomes very intensive again at the two sites. This is probably linked to small-scale synoptic weather changes with the advection of cold air. The model was set not to simulate cooling rates on days with large-scale synoptic weather changes, i.e. with a daily air pressure change >10 hPa. This means that the present version of the model is restricted to steady synoptic weather conditions at both small and large scales.

4.2. Mean profile evaluation

The mean profiles of modelled and observed cooling rates for two open sites (GOT098 and GOT092) and three dense sites (GOT039, GOT040 and LDN046) for the three weather conditions, described by the 25th percentile of CRIF, inter-percentile and 75th percentile, are shown in Figure 11. The three classes can indicate roughly clear and calm (ideal) conditions, semi-cloudy and light-wind conditions, cloudy and windy conditions, respectively. GOT092, GOT040 and LDN046 are independent datasets, which were not used for the model development. The statistical performance was evaluated using the co-efficient of determination (R^2), root mean square error (RMSE) and mean bias error (MBE), which were calculated for all the modelled data points of the number N (Table 1). However, for the different lengths of nights from May to September, the modelled cooling rates were plotted only at the time when the number of the data points was larger than half of the observational data points.

The model simulates cooling rates well for all the sites. The standard deviations (shown by vertical bars), indicating the variation of cooling rates from day to day, show similar patterns between the model and the observation. From the profiles of

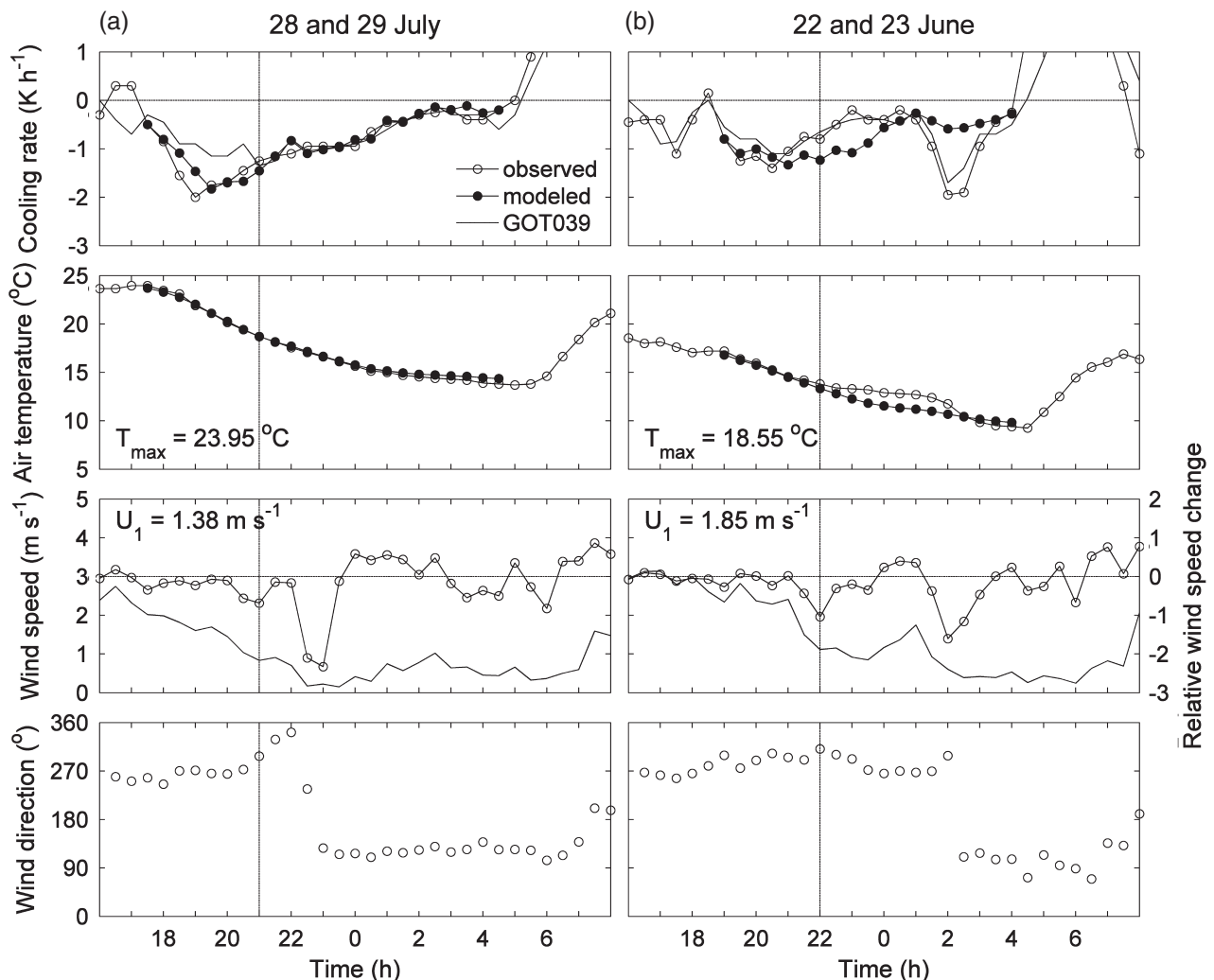


Figure 10. Nocturnal profiles of modelled (black point), observed (grey circle) cooling rate and air temperature, wind speed (black line), relative wind speed change (circle), wind direction for 28 July (a) and 22 June (b) in 1999 for an open site (GOT098) in Gothenburg. In order to see the start time of Phases 1A and 2 in the observation, cooling rate for a built-up site (GOT039) is drawn together (light grey line). Maximum daily air temperature (T_{\max}) and average wind speed (U_1) for ± 3 h around the estimated time of the most intensive cooling are shown.

GOT098 (1st column, Figure 11), it is seen clearly that the magnitude of cooling rates is simulated to be large under clear and calm conditions and smaller under cloudier and windier conditions. The two phases in cooling are modelled also as less distinct under cloudier and windier conditions. RMSE of cooling rates (Table 1) is low, ranging from 0.36 to 0.53 K h⁻¹, while R^2 is not very high, e.g. 0.52 under clear conditions. R^2 is lower under cloudier and windier conditions. This is because the relative magnitude of the errors in the modelled cooling rates is not only larger under cloudier and windier conditions but also because changes in clouds during night are more likely to occur under cloudier and windier conditions. The model cannot simulate the impact of temporal changes in clouds on cooling rates yet due to the lack of cloud data during night. MBEs from 0.063 to 0.067 K h⁻¹ indicate that there are slightly systematic errors where the model tends to under-estimate the magnitude of cooling rates. In comparison with GOT039 (3rd column), the model produces successfully the magnitude of cooling rates in Phase 1 with the low SVF under all the weather conditions, though cooling rates around sunset are slightly over-estimated under clear and calm conditions. With slightly lower R^2 under clear and calm conditions as well as semi-cloudy and light-wind conditions but lower RMSE

than those for GOT098, the performance is more or less the same. MBEs are also similar. In comparison with GOT092 and GOT040 (2nd and 4th columns), their performances are more or less the same as those for GOT098 and GOT039. Under clear and calm conditions, the performances are slightly poorer than those for GOT098 and GOT039 with lower R^2 and higher RMSEs. The results are expected as the datasets of GOT092 and GOT040 are independent of the model setting. Also, for LDN046 (5th column), which is a built-up site located in London, the modelled cooling rates agree with the observation. The statistical performance is similar to GOT040, though with relatively large MBEs for semi-cloudy and light-wind conditions as well as cloudy and windy conditions. Nevertheless, it is suggested that the model is able to simulate cooling rates at other sites with complex urban geometry and in other cities with similar climate zones.

Air temperature calculated using the modelled cooling rates corresponds with the observations. The statistical performance for GOT098 and GOT039 is $R^2 \geq 0.87$, RMSE $\leq 1.54^{\circ}\text{C}$ and $-0.31 \leq \text{MBE} \leq 0.7^{\circ}\text{C}$ (Table 1). Those for the evaluation sites (GOT092, GOT040 and LDN046) are about the same, though R^2 for LDN046 under cloudy and windy conditions is slightly lower.

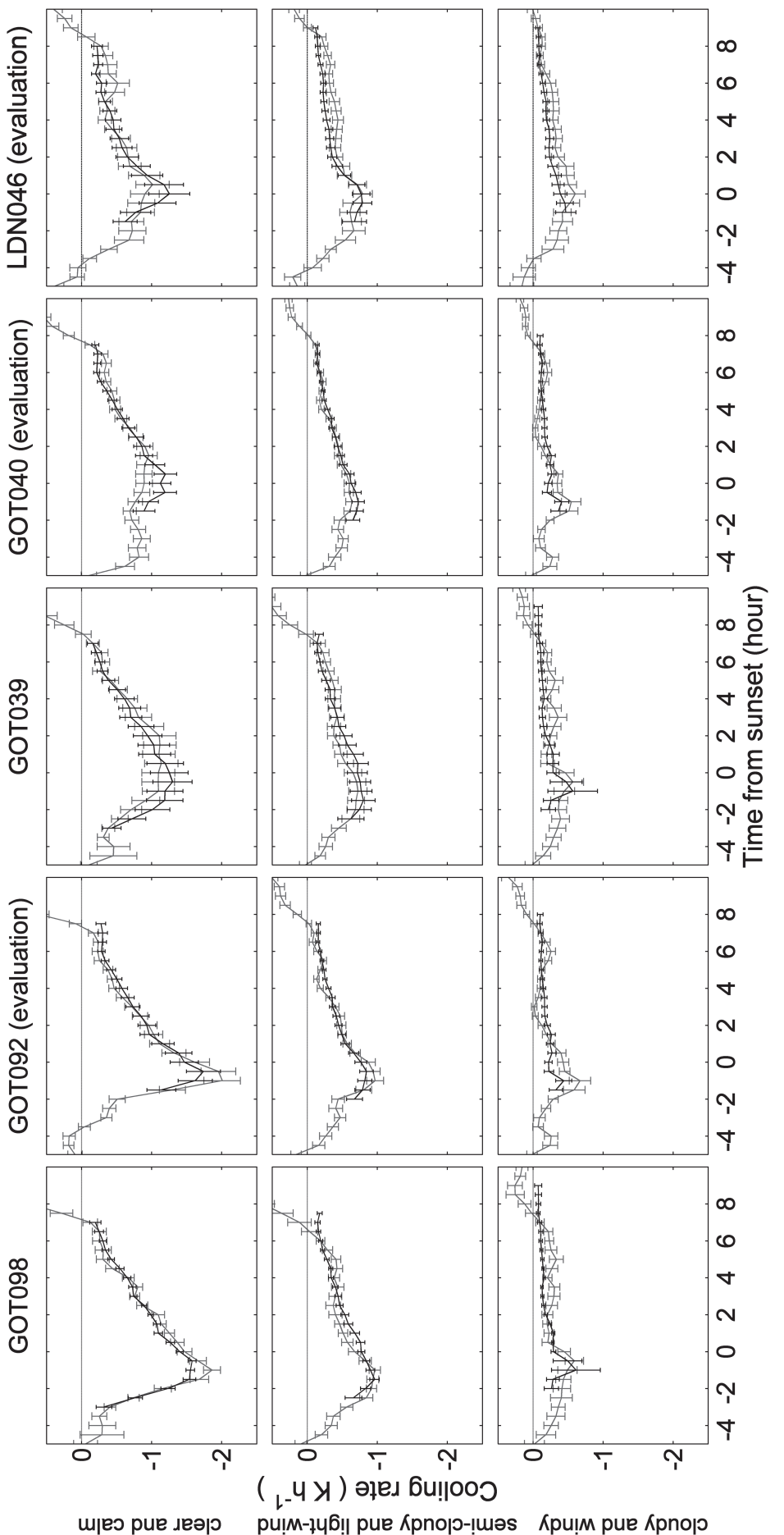


Figure 11. Average profiles of modelled (black) and observed (grey) cooling rates for two open sites (GOT098 and GOT092), two built-up sites (GOT039, GOT040) in Gothenburg and one built-up site (LDN046) in London for three weather conditions (upper row: clear and calm condition, middle: semi-cloudy and light-wind, lower: cloudy and windy) classified by the cooling rate impact factor (25^{th} percentile, inter-percentile and 75^{th} percentile, respectively). For the different lengths of nights between May and September, the modelled cooling rates were plotted only at the time when the number of the data points was larger than half of the observational data points. Vertical bars on the profiles show the standard deviations of cooling rates at the time.

Table 1. Statistical performance of modelling cooling rate (CR) and air temperature (T_a) for two open sites (GOT098 and GOT092) and two built-up sites (GOT039 and GOT040) in Gothenburg and for one built-up site (LDN046) in London for three weather conditions (upper row: clear and calm condition, middle: semi-cloudy and light-wind, lower: cloudy and windy) classified by cooling rate impact factor (25th quartile, interquartile, and 75th quartile, respectively). Statistics are calculated for N data points on the number of days shown in the parenthesis.

Weather conditions	GOT098		GOT092 (evaluation)		GOT039		GOT040 (evaluation)		LDN046 (evaluation)	
	CR	T_a	CR	T_a	CR	T_a	CR	T_a	CR	T_a
Clear and calm	N (days)	460 (22)		1248 (66)		460 (22)		1248 (66)		383 (19)
	R^2	0.52	0.93	0.49	0.86	0.41	0.94	0.22	0.84	0.26
	RMSE	0.51	1.35	0.54	1.33	0.40	1.12	0.44	1.44	0.42
	MBE	0.064	0.36	0.006	-0.028	0.007	-0.31	-0.047	-0.71	-0.0025
Semi-cloudy and light-wind	N (days)	645 (32)		2037 (105)		645 (32)		2116 (105)		919 (41)
	R^2	0.23	0.87	0.26	0.81	0.16	0.90	0.20	0.89	0.19
	RMSE	0.53	1.54	0.55	1.54	0.45	1.24	0.42	1.14	0.39
	MBE	0.067	0.29	0.014	0.13	0.055	0.70	-0.0092	-0.18	0.11
Cloudy and windy	N (days)	242 (12)		466 (23)		255 (12)		449 (23)		421 (19)
	R^2	0.35	0.95	0.11	0.91	0.39	0.96	0.12	0.94	0.37
	RMSE	0.36	0.93	0.32	0.92	0.32	0.84	0.28	0.75	0.28
	MBE	0.063	0.44	0.028	0.21	0.053	0.34	0.017	0.087	0.10

MBE, mean bias error; RMSE, root mean square error.

5. Discussion

5.1. Overall model performance

Overall, the model simulates nocturnal cooling rates well. The model successfully captures the two-phase cooling in terms of the magnitude as well as the start times of Phase 1 (t_1) and 2 (t_2). However, the statistics in the model evaluation also show that there is room for model improvement. Slightly positive MBEs of cooling rates for all CRIF cases as well as for both GOT098 and GOT039 indicate not only systematic errors of the under-estimation but also imply that the cause is not related to the estimation of the impact of prevailing weather conditions and SVF on cooling rates, i.e. CRIF and SVIF. For air temperature calculated from the modelled cooling rates at the three independent sites (GOT092, GOT040 and LDN046) (Table 1), RMSEs range from 0.74 to 1.54 °C, MBEs from -0.71 to 0.70 °C and R^2 from 0.78 to 0.94 under clear and calm conditions. Here, the model performance is compared with the performance of the canopy air temperature (CAT) model presented by Erell and Williamson (2006) and the performance of the urban weather generator by Bueno *et al.* (2013). Even though they did not present the model performance separately during daytime and night time, the absolute errors of night time air temperature roughly estimated from their figures are about 1–2 °C and sometimes higher, particularly before sunrise. Comparing them with the MBEs, it is concluded that the present model has a better performance for night time but requires less input data and lower computer resources. Air temperature differences of up to 3–4 °C between open and nearby dense sites have been recorded previously under clear and calm conditions in Gothenburg (Eliasson, 1996b; Thorsson and Eliasson, 2003). In the city of London, where more complex urbanization occurs, the intra-urban spatial variation in air temperature is expected to be larger. With this information, it is suggested that the model is capable of simulating the intra-urban spatial variation of night time air temperature.

5.2. Timing of phases

The timing of t_1 and t_2 was successfully detected by using relative wind speed change that can indicate changes in the structure

of the turbulence. The advantage of using relative wind speed change is that it requires only wind speed measured by standard anemometers installed at most meteorological stations. In other words, high-frequency wind speed is not required to detect the transition of turbulence. On some days, the estimated timing of t_{peak} was shifted compared with the observation time. A possible reason was that the timing was simply estimated to be in the middle, between t_1 and t_2 . The t_{peak} value was found to correspond to the time when Ri_b turns from negative to positive (Section 3.5). The use of Ri_b could improve the estimation of t_{peak} . In the present model, Ri_b was not used as the calculation requires air temperature at two levels, which are not often available. Instead of Ri_b , other atmospheric stability indices could be used, e.g. ζ ($= z/L$), a surface-layer scaling parameter using the Obukhov length L . It requires turbulent fluxes, which might be even harder to obtain from standard meteorological measurements, but they can be calculated by surface energy balance models.

5.3. Cooling rate impact factor

CRIF was introduced to indicate the degree of a reduction in CR_{peak} under prevailing weather conditions (described by CI and U) referred to under an ideal condition (CI = 1 and $U = 0$). It was shown that CRIF was approximately linearly related to CR_{peak} . CRIF was developed based on the analogy with the weather factor of Oke (1998) that consists of wind speed and cloud cover/type. However, the advantage of CRIF is that the calculation of CI requires only standard meteorological information such as global radiation, air temperature, relative humidity and air pressure and that the influence of $U < 1 \text{ m s}^{-1}$ on CR_{peak} is taken into account. Another strength of CRIF is that the relationship between CR_{peak} and other factors can be simplified by using CRIF, e.g. the relationship between CR_{peak} and T_{max} in Figure 7. The concept of using such impact factors can be applied to the parameterization of other influences on cooling rates (see Section 5.6).

5.4. Sky view impact factor

The impact of SVF on CR_{peak} depending on CRIF is estimated successfully using SVIF in the model as the model performance

is more or less the same between open sites and built-up sites. However, it was found to be under-estimated slightly under clear and calm conditions (Figure 11). A possible reason is that the linear relationship between SVIF and SVF was distributed equally in the CRIF range from 0 to 1. It is not certain that the impact of SVF on CR_{peak} increases linearly with CRIF. Although SVIF uses the average of SVFs within the source area of a site calculated using DSMs, the SOLWEIG model and the ArcMap software, the complex process of determining SVF could be a practical disadvantage. SVF can be also determined by analysing fisheye-lens photographs of the hemispherical environment (Steyn, 1980) unless the neighbourhood is totally different from the study site. Other alternatives used as a measure of building density could be H/W or the ratio of mean building height to the fraction of ground surfaces, but none of them are obtained easily either.

5.5. Impact of wind disturbance

The model captured the impact of disturbance caused by changes in wind speed on cooling rates in every time step. Especially in Phase 2, modelled fluctuations had a better agreement with the observations compared with Phases 1A and 1B (Figure 10). The simple scheme of $\Delta CR_w(t)$ (shown in Section 3.5) was developed under the assumption that the atmosphere is unstable in Phase 1A and stable in Phases 1B and 2. However, while the atmosphere is strongly stabilized in Phase 2, it is in transition from unstable to stable in Phases 1A and 1B. Thus, the vertical thermal stratification of the atmosphere in Phases 1A and 1B is not as strong as in Phase 2, and the thermal stratification is more likely to be opposite to the assumption in Phases 1A and 1B. In this case, the scheme can fail, and it might contribute to the systematic errors (the slightly positive MBEs). The same thing can happen under cloudier conditions when the thermal stratification tends to be weaker. This problem is potentially improved by introducing information about the atmospheric stability in every time step. Additionally, synoptic wind changes or the advection of either warmer or cooler air (depending on the thermal conditions in the surroundings) make it difficult to estimate $\Delta CR_w(t)$. Despite that, the scheme is confirmed to capture the influence of wind disturbance in most cases.

5.6. Other factors affecting cooling rates

There are several other factors that are not considered in the model, e.g. the heterogeneity of surface materials, evapotranspiration from vegetation, the release of anthropogenic heat, air humidity and advection of cooler/warmer air from surroundings. Oke (1981) and Konarska *et al.* (2015a) suggest that SVF explains >80% of the spatial variation of UHI/IUHI intensities or cooling rates; thus, the residual percent can be explained by those factors.

The types of surface materials can affect cooling rates largely as the radiation properties (albedo and emissivity) influence long-wave radiation divergence, and their thermal admittances determine the amount of heat released from the surface into the atmosphere when a temperature difference between the surface and the atmosphere exists (Oke, 1988; Oke *et al.*, 1991). In the present study, such effects were not considered as the study sites are constructed with dark-coloured, standard urban fabrics (asphalt and brick), which have almost the same value of thermal admittance (referred to table 7.4 of Oke, 1987). However, the effects might not be neglected when the model is tested for sites with other materials, e.g. concrete, stone and grass. The role of soil moisture content in nocturnal cooling of the atmosphere is

complex. While an increase in soil moisture enhances cooling due to evaporation, it diminishes cooling due to increased thermal admittance (Oke, 1987).

The effect of evapotranspiration on nocturnal cooling has been reported at vegetated sites in Ouagadougou, Burkina Faso (Holmer *et al.*, 2013) and Gothenburg, Sweden (Konarska *et al.*, 2015a). The cooling rates at vegetated sites in Ouagadougou were almost twice more than sparsely vegetated sites (Holmer *et al.*, 2013).

In other climate zones (e.g. tropical climate), air humidity can also be an important factor as long-wave radiative divergence and evapotranspiration from vegetation vary with the emissivity and vapour pressure deficit in the air (Konarska *et al.*, 2015b). However, with the same level of air moisture, the model can be applied to other climate zones as it takes into account sensible heat and long-wave radiative fluxes related to high solar insolation using T_{max} (Figure 7).

Cooling during winter is less intensive for the release of anthropogenic heat and less vegetation. The importance of anthropogenic heat on UHI/IUHI intensities and cooling rates has been emphasized by many previous studies (e.g. Arnfield, 2003; Fan and Sailor, 2005; Offerle *et al.*, 2006). Ryu and Baik (2012) showed, using a meso-scale atmospheric model, that anthropogenic heat contributes to the UHI intensity more than impervious surface and urban density/geometry. In order to use the cooling rate model with cold seasons, the impact of anthropogenic heat has to be taken into account as its contribution to surface energy balance becomes relatively large in winter.

A simple way to take into account the influences of these factors is to parameterize their contributions to cooling rates as it was done for the prevailing weather conditions and SVF by introducing the impact factors, CRIF and SVIF, respectively. More precisely, the model coupling with an urban land surface model derives sensible and latent heat fluxes from the surface into the atmosphere considering most of those factors, such as different surface properties, evapotranspiration from vegetation and anthropogenic heat.

5.7. Future development

A suggestion provided by the present study is that the model should be tested for other cities, preferably in lower latitudes with different climate classes and/or different site characteristics, especially different surface materials. Although the model was tested with independent datasets in the same city and one other city, some parts of the model setting described in Section 3 were statistically or empirically determined, probably with regional dependencies. For further model development, the model is designed so that users can easily change and test empirical parameters for other cities.

The coupling of the model to other models, e.g. urban energy balance/building energy balance models, enables the model to take into account the impact of other factors influencing cooling rates.

6. Conclusions

The nocturnal cooling rate model (NOCRAM) was developed empirically to represent specifically that the temporal development of nocturnal cooling progresses in two distinct phases at open sites and built-up sites under a wide range of weather conditions in warm months. The model requires commonly used meteorological variables (i.e. wind speed, incoming short-wave

radiation, air temperature, relative air humidity, air pressure) from a reference meteorological station as well as the geometric information (i.e. the sky view factor (SVF) of the site and the geographical co-ordinates of the reference station). The model simulated cooling rates well, capturing the characteristic development of the two-phase cooling under different weather conditions as well as the influence of wind disturbance. Using the modelled cooling rates, the temporal development of nocturnal air temperature was calculated with sufficient accuracy to capture its intra-urban spatial variation. Future model development will include the impacts of other surface materials, anthropogenic heat and evapotranspiration on cooling rates. The model should also be tested in other cities with different site characteristics and/or different climate zones. Due to its simplicity, the model can be used easily in climate applications, such as nocturnal human thermal comfort estimation and climate-sensitive urban planning and design.

Acknowledgements

This project is supported financially by the Swedish Research Council Formas, the Swedish Energy Agency, the Swedish Environmental Protection Agency, the Swedish National Heritage Board and the Swedish Transport Administration (214-2010-1706 and 250-2010-358). Dr. Janina Konarska is appreciated for operating the intra-urban air temperature measurement during 2012–2014 as are Mr. William Morrison and Dr. Simone Kotthaus for providing observational data from London and Dr. David Rayer for the helpful advice and comments on the manuscript.

Supporting information

The following material is available as part of the online article:

Figure S1. Frequency of time difference (h) between when cooling rate for the open site ($SVF = 0.98$) is the most intensive and when the sign of Rib changes from negative to positive, in Gothenburg during May–September 1999.

References

- Acevedo OC, Fitzjarrald DR. 2001. The early evening surface-layer transition: temporal and spatial variability. *J. Atmos. Sci.* **58**: 2650–2667.
- Acevedo O, Fitzjarrald D. 2003. In the core of the night-effects of intermittent mixing on a horizontally heterogeneous surface. *Bound.-Layer Meteorol.* **106**: 1–33.
- Arnfield AJ. 2003. Two decades of urban climate research: a review of turbulence, exchanges of energy and water, and the urban heat island. *Int. J. Climatol.* **23**: 1–26.
- Bohnstengel SI, Evans S, Clark PA, Belcher SE. 2011. Simulations of the London urban heat island. *Q. J. R. Meteorol. Soc.* **137**: 1625–1640.
- Bueno B, Norford L, Hidalgo J, Pigeon G. 2013. The urban weather generator. *J. Bldg. Perf. Sim.* **6**: 269–281.
- Chow WTL, Roth M. 2006. Temporal dynamics of the urban heat island of Singapore. *Int. J. Climatol.* **26**: 2243–2260.
- Crawford TM, Duchon CE. 1999. An improved parameterization for estimating effective atmospheric emissivity for use in calculating daytime downwelling longwave radiation. *J. Appl. Meteorol.* **38**: 474–480.
- Davenport AG. 1960. Rationale for determining design wind velocities. *J. Struct. Eng. ASCE* **86**: 39–68.
- Eliasson I. 1994. Urban-suburban-rural air temperature differences related to street geometry. *Phys. Geogr.* **15**: 1–22.
- Eliasson I. 1996a. Urban nocturnal temperatures, street geometry and land use. *Atmos. Environ.* **30**: 379–392.
- Eliasson I. 1996b. Intra-urban nocturnal temperature differences: a multivariate approach. *Clim. Res.* **7**: 21–30.
- Erell E, Williamson T. 2006. Simulating air temperature in an urban street canyon in all weather conditions using measured data at a reference meteorological station. *Int. J. Climatol.* **26**: 1671–1694.
- Fan H, Sailor DJ. 2005. Modeling the impacts of anthropogenic heating on the urban climate of Philadelphia: a comparison of implementations in two PBL schemes. *Atmos. Environ.* **39**: 73–84.
- Golder D. 1972. Relations among stability parameters in the surface layer. *Bound.-Layer Meteorol.* **3**: 47–58.
- GVC. 2014. Meteorological database operated by the Department of Earth Sciences, University of Gothenburg. http://gvc.gu.se/english/climate_stations/climate-data (accessed 10 November 2014).
- Harman IN, Belcher SE. 2006. The surface energy balance and boundary layer over urban street canyons. *Q. J. R. Meteorol. Soc.* **132**: 2749–2768.
- Holmer B, Thorsson S, Eliasson I. 2007. Cooling rates, sky view factors and the development of intra-urban air temperature differences. *Geogr. Ann. Ser. A Phys. Geogr.* **89A**: 237–248.
- Holmer B, Thorsson S, Lindén J. 2013. Evening evapotranspirative cooling in relation to vegetation and urban geometry in the city of Ouagadougou, Burkina Faso. *Int. J. Climatol.* **33**: 3089–3105.
- Johnson DB. 1985. Urban modification of diurnal temperature cycles in Birmingham, U.K. *Int. J. Climatol.* **5**: 221–225.
- Kawamura T. 1964. Analysis of the temperature distribution in the Kumagaya city – a typical example of the urban climate of a small city. *Tokyo J. Climatol.* **1**: 74–78.
- Kidder SQ, Essenwanger OM. 1995. The effect of clouds and wind on the difference in nocturnal cooling rates between urban and rural areas. *J. Appl. Meteorol.* **34**: 2440–2448.
- Konarska J, Homer B, Lindberg F, Thorsson S. 2015a. Influence of vegetation and building geometry on the spatial variations of air temperature and cooling rates in a high latitude city. *Int. J. Climatol.* DOI: 10.1002/joc.4502.
- Konarska J, Uddling J, Holmer B, Lutz M, Lindberg F, Pleijel H, et al. 2015b. Transpiration of urban trees and its cooling effect in a high latitude city. *Int. J. Biometeorol.* **60**: 159–172, DOI: 10.1007/s00484-015-1014-x.
- Kuttler W, Barlag A-B, Robmann F. 1996. Study of the thermal structure of a town in a narrow valley. *Atmos. Environ.* **30**: 365–378.
- Laaidi K, Zeghnoun A, Dousset B, Bretin P, Vandentorren S, Giraudet E, et al. 2012. The impact of heat islands on mortality in Paris during the August 2003 heat wave. *Environ. Health Perspect.* **120**: 254–259.
- Lindberg F, Grimmond CSB. 2010. Continuous sky view factor maps from high resolution urban digital elevation models. *Clim. Res.* **42**: 177–183.
- Lindberg F, Grimmond CSB. 2011a. Nature of vegetation and building morphology characteristics across a city: influence on shadow patterns and mean radiant temperatures in London. *Urban Ecosyst.* **14**: 617–634.
- Lindberg F, Grimmond CSB. 2011b. The influence of vegetation and building morphology on shadow patterns and mean radiant temperatures in urban areas: model development and evaluation. *Theor. Appl. Climatol.* **105**: 311–323.
- Lindberg F, Holmer B, Thorsson S. 2008. SOLWEIG 1.0 – Modelling spatial variations of 3D radiant fluxes and mean radiant temperature in complex urban settings. *Int. J. Biometeorol.* **52**: 697–713.
- London Urban Micromet data Archive (LUMA). 2014. BFCL and BCT. <http://www.met.reading.ac.uk/micromet/LUMA/LUMA.html> (accessed 4 December 2014).
- Magee N, Curtis J, Wendler G. 1999. The urban heat island effect at Fairbanks, Alaska. *Theor. Appl. Climatol.* **64**: 39–47.
- Moreno-Garcia MC. 1994. Intensity and form of the urban heat island in Barcelona. *Int. J. Climatol.* **14**: 705–710.
- Morris CJG, Simmonds I, Plummer N. 2001. Quantification of the influences of wind and cloud on the nocturnal urban heat island of a large city. *J. Appl. Meteorol.* **40**: 169–182.
- Offerle B, Grimmond CSB, Fortuniak K, Klýšek K, Oke TR. 2006. Temporal variations in heat fluxes over a central European city centre. *Theor. Appl. Climatol.* **84**: 103–115.
- Oke TR. 1981. Canyon geometry and the nocturnal urban heat island: comparison of scale model and field observations. *J. Climatol.* **1**: 237–254.
- Oke TR. 1987. *Boundary Layer Climates*, 2nd edn. Routledge: London and New York.
- Oke TR. 1988. The urban energy-balance. *Prog. Phys. Geogr.* **12**: 471–508.
- Oke TR. 1998. An algorithmic scheme to estimate hourly heat island. *Second Urban Environment Symposium*, 2–5 November 1998, Boston, MA, American Meteorological Society; 80–83.

- Oke T, Johnson G, Steyn D, Watson I. 1991. Simulation of surface urban heat islands under 'ideal' conditions at night part 2: diagnosis of causation. *Bound.-Layer Meteorol.* **56**: 339–358.
- Oke TR, Maxwell GB. 1975. Urban heat island dynamics in Montreal and Vancouver. *Atmos. Environ.* **9**: 191–200.
- Rocklöv J, Ebi K, Forsberg B. 2011. Mortality related to temperature and persistent extreme temperatures: a study of cause-specific and age-stratified mortality. *Occup. Environ. Med.* **68**: 531–536.
- Runnalls KE, Oke TR. 2000. Dynamics and controls of the near-surface heat island of Vancouver, British Columbia. *Phys. Geogr.* **21**: 283–304.
- Ryu Y-H, Baik J-J. 2012. Quantitative analysis of factors contributing to urban heat island intensity. *J. Appl. Meteorol. Climatol.* **51**: 842–854.
- Spronken-Smith RA, Oke TR. 1998. The thermal regime of urban parks in two cities with different summer climates. *Int. J. Remote Sens.* **19**: 2085–2104.
- Statistics Sweden (SCB). 2014. Befolkningsstäthet (invånare per kvadratkilometer), folkmängd och landareal efter region och kön. År 1991–2014. <http://www.statistikdatabasen.scb.se/pxweb/sv/ssd/> START_BE_BE0101_BE0101C/BefArealTathetKon/?rxid=6a7981e4-9d22-4d57-be0b-a2ca53b8e971 (accessed 16 April 2015).
- Steyn DG. 1980. The calculation of view factors from fisheye-lens photographs: research note. *Atmos. Ocean* **18**: 254–258.
- Sundborg Å. 1951. Climatological studies in Uppsala with special regard to the temperature conditions in the urban area. *Geographica* **22**: 111.
- Swaid H, Hoffman ME. 1990. Prediction of urban air temperature variations using the analytical CTTC model. *Energy Build.* **14**: 313–324.
- Thorsson S, Eliasson I. 2003. An intra-urban thermal breeze in Göteborg, Sweden. *Theor. Appl. Climatol.* **75**: 93–104.
- Thorsson S, Rocklöv J, Konarska J, Lindberg F, Holmer B, Dousset B, et al. 2014. Mean radiant temperature – a predictor of heat related mortality. *Urban Clim.* **10**: 332–345.
- Unger J. 2004. Intra-urban relationship between surface geometry and urban heat island: review and new approach. *Clim. Res.* **27**: 253–264.
- Upmanis H, Eliasson I, Lindqvist S. 1998. The influence of green areas on nocturnal temperatures in a high latitude city (Göteborg, Sweden). *Int. J. Climatol.* **18**: 681–700.